



Effects of different defective linkers on the photocatalytic properties of Cu-BTC for overall water decomposition

Li Zhang, Changyan Guo^{*}, Tingxiang Chen, Yuan Guo, Afaq Hassan, Yuli Kou, Cheng Guo, Jide Wang^{*}

Key Laboratory of Oil and Gas Fine Chemicals, Ministry of Education & Xinjiang Uygur Autonomous Region, School of Chemical Engineering and Technology, Xinjiang University, Urumqi, China



ARTICLE INFO

Keywords:
Metal-Organic Frameworks
Bifunctional catalyst
Defective linker
Photocatalysis
Water splitting

ABSTRACT

This manuscript proposed a synthesis strategy for simultaneously constructing defect structure and mixed valence coordinated unsaturated sites (CUS) in Cu-BTC ($\text{BTC}=1,3,5\text{-trihydroxybenzene}$) framework. Different defective linkers with increasing pK_a value were used to regulate the defect concentration and $\text{Cu}^{1+}/\text{Cu}^{2+}$ CUS content. The pK_a value of defective linkers was proved to be inversely proportional to the defect concentration and $\text{Cu}^{1+}/\text{Cu}^{2+}$ CUS content. Compared with pure Cu-BTC, the defective Cu-BTC samples have obviously improved specific surface area, light absorption, bandgap, and charge carrier separation rate. All of these advantages make defective variants become an excellent bifunctional overall water splitting catalyst with O_2 and H_2 generation rates of $3942 \mu\text{mol}\cdot\text{g}^{-1}\cdot\text{h}^{-1}$ and $15107 \mu\text{mol}\cdot\text{g}^{-1}\cdot\text{h}^{-1}$, respectively. Although the defective linkers with small pK_a value can create more defects, excessive defects in framework will lead to the parent structure collapse, and can also serve as recombination centers to reduce the photocatalytic activity of materials.

1. Introduction

With the aggravation of energy shortage and environmental problems caused by the consumption of fossil energy, solar energy, as a new energy with environmental protection and pollution-free, has been vigorously developed [1]. Among which, solar-driven water splitting is a highly attractive approach to convert solar energy into chemical fuels [2]. Metal-organic frameworks (MOFs), as a new class of porous materials, have received much attention in the field of photocatalytic water splitting owing to their outstanding properties such as high surface area, tunable porosity, adjustable pore channels and excellent design flexibility [3,4]. Horiuchi et al. synthesized a Pt/Ti-MOF-NH₂ photocatalyst, and the ESR investigation indicates that the electrons can be transferred from the organic ligand to Pt nanoparticles via titanium-oxo clusters [5,6]. Relevant researches also suggest that the carriers can move between the metal and the ligand to facilitate high-efficient separation of electron-hole pairs. Meanwhile, the metal sites isolated via organic ligands in MOFs can be considered as quantum dots to shorten the diffusion length of charge carriers [7]. The present studies confirm that the specific surface area and bandgap of MOFs materials can be regulated by tuning the coordination environment of organic ligands and/or

metal centers to improve their performance [8,9]. Defect engineering is an attractive strategy for tuning the coordination environment of MOFs materials.

The defect in MOFs is described as sites (e.g. ligands, clusters) deviating from an ideally ordered crystal structure due to modified or missing secondary building units (SBUs). Various properties of MOFs, such as (micro/mesoporous) porosity, active sites, bandgap structure, etc., can be adjusted by defect engineering [10,11]. Especially in the field of photocatalysis, defect engineering is a desirable strategy to improve the efficiency of light capture and carrier separation [12,13]. Fischer et al. synthesized a defective HKUST-1 with the coordinated unsaturated Cu^{1+} sites and two different types of defects (modified paddlewheels and missing paddlewheels) by introducing isophthalate. The electronic and spatial modification on the CUS can expand the coordination space near the metal sites [14]. Li and coworkers synthesized Mn-MOF-74 with controllable defect concentration via introducing modulators with reduced coordination numbers. It was found that the chemical form and coordination group number of the modulators have significant effect on the defect concentration in MOFs structure [15]. Hmadeh et al. effectively regulated and controlled the defect concentration in UiO-66 framework by varying the type and amount of the

* Corresponding authors.

E-mail addresses: gcywlw@xju.edu.cn (C. Guo), awangjd@sina.cn (J. Wang).

modulator. Their study confirms that the modulator with greater deprotons capacity (lower pK_a value) has higher deprotonation ability, resulting in the formation of more defects in the structure [16]. Our previous work found that systemically doped defective linker (vanillin) can construct copper-ion vacancies and mixed-valence $\text{Cu}^{1+}/\text{Cu}^{2+}$ sites in Cu-BTC framework [17]. All the above results show that the types and properties of modulator have significant impact on the photocatalytic properties of materials. It is necessary to regulate the specific properties of materials by selecting different defective linkers and controlling the defect concentration.

Herein, a series of defective Cu-BTC were synthesized by introducing different defective linkers (defective linkers have fewer coordination sites compared to the parent linker) into the Cu-BTC structure via mixed-component method. Compared with pure Cu-BTC, defective Cu-BTC samples have obviously improved characteristics, such as the specific surface area, the electronic and spatial properties of CUS, light absorptivity, bandgap, and charge carrier separation rate. The introduction of defective linkers can not only form defects in the structure, but also lead to partial reduction of Cu^{2+} to form mixed-valence CUS. The mixed-valence $\text{Cu}^{1+}/\text{Cu}^{2+}$ CUS can regulate the bandgap of metal active centers and improve the carrier separation/transfer rate. Therefore, the defective Cu-BTC catalysts show more excellent photocatalytic water splitting performance than that of pure Cu-BTC. Besides, it has been proved that the defect content is inversely proportional to the pK_a value of the defective linkers. The appropriate defect contents can improve the photocatalytic performance of the material, while the excessive defects may serve as the recombination sites of the electron-hole pairs to decrease the photocatalytic performance.

2. Experimental Section

2.1. Sample preparation

Copper nitrate trihydrate ($\text{Cu}(\text{NO}_3)_2 \cdot \text{H}_2\text{O}$), Benzenetricarboxylic acid (H_3BTC), 3-Formylbenzoic acid (3-FBA), 3-Hydroxybenzoic acid (3-HBA), 3-Aminobenzoic acid (3-ABA), Isophthalic acid (IPA), N,N-Dimethylformamide (DMF) and methanol were purchased from Adamas-beta, Innochem and Sigma-Aldrich. All reagents are analytical and are used without further purification. The distilled water used in the experiment was prepared with a distilled water purification system.

2.2. Synthesis of Samples

Pure Cu-BTC was synthesized according to the reported method [18]. The defective Cu-BTC samples were prepared according to following procedure. H_3BTC (1 mmol) and $\text{Cu}(\text{NO}_3)_2 \cdot \text{H}_2\text{O}$ (1.5 mmol) were dissolved in 30 mL solution with DMF:EtOH:H₂O (1:1:1 (v/v/v)). When the above solution form a uniform blue solution, 10 mL solution containing the defective linker (10 mmol) was added. The mixture was stirred for 15 min and then transferred into a 100 mL Teflon-sealed and bake in a 100 °C oven for 12 h. The powder was collected by centrifugation, wash and dry. Defective Cu-BTC samples formed by different defective linkers are named as follows: Cu-BTC-FBA (3-FBA as the defective linker); Cu-BTC-HBA (3-HBA as the defective linker); Cu-BTC-ABA (3-ABA as the defective linker); Cu-BTC-IPA (IPA as the defective linker).

2.3. Characterization of samples

The morphology was observed via a FEI Magellan 400 L XHR Field mission Scanning Electron Microscope (SEM). X-ray diffraction (XRD) patterns were obtained using a Rigaku D/max-ga X-ray diffractometer with Cu K α radiation, which were recorded in the 2 θ range of 5–80° with a scan rate of 6°/min. FT-IR spectra were recorded by a Bruker EQUINOX-55 FTIR instrument in a wavenumber range of 400–4000 cm⁻¹ at room temperature. X-ray photoelectron spectroscopy (XPS) was conducted on Thermo K-Alpha⁺ X-ray photoelectron spectrometer

equipped with the monochromatic Al K α (1486.8 eV) source. The electron paramagnetic resonance spectra (CW EPR) were recorded on the Bruker A300 instrument. It operates at X-band frequencies and a 100 kHz field modulation, which is equipped with a cylindrical cavity. The surface area was calculated via N_2 adsorption-desorption isotherm measurements on an Autosorb iQ instrument, and pore size distribution were estimated through the analysis of the desorption portion of the isotherms using the DFT method. Thermogravimetric analysis (TGA) was carried out under a N_2 atmosphere at a heating rate of 10 °C/min up to 500 °C on the Shimadzu DTG-50 thermal analyzer. The UV-vis absorption spectra were acquired by using a UV-2550 spectrophotometer (Shimadzu). The Photoluminescence (PL) spectra were obtained on the FLS920 full-function steady-state/transient fluorescence spectrometer. UV-vis diffuse reflectance spectra (UV-vis DRS) recorded on a Unico UV-4802S, and barium sulfate was used as the reference.

2.4. Photocatalytic reaction

The photocatalytic activity of samples was studied in the water oxidation system and water reduction system. The typical light-driven oxygen evolution reaction: catalyst (3–7 mg), $\text{Na}_2\text{S}_2\text{O}_8$ (10–40 mM) and NaOH (0.01–1 mM) solution were added to a reaction vessel. The typical light-driven hydrogen evolution reaction: catalyst (1–5 mg), EY dye (3–9 mg), TEOA (5%–15%) and distilled water were added to a reaction vessel. The reaction flask was sealed with a rubber septum and purged with argon gas for 10 min. The photocatalytic reaction was carried out by a 300 W Xe lamp equipped with a long-pass filter ($\lambda \geq 420$ nm). The produced gases were analyzed by gas chromatography instrument (SHIMADZU GC-2014 C) with a thermal conductivity detector (TCD, 5 Å molecular sieve column) and a column dimension (2 m × 4 mm), Ar as the carrier gas.

2.5. Electrochemistry measurements

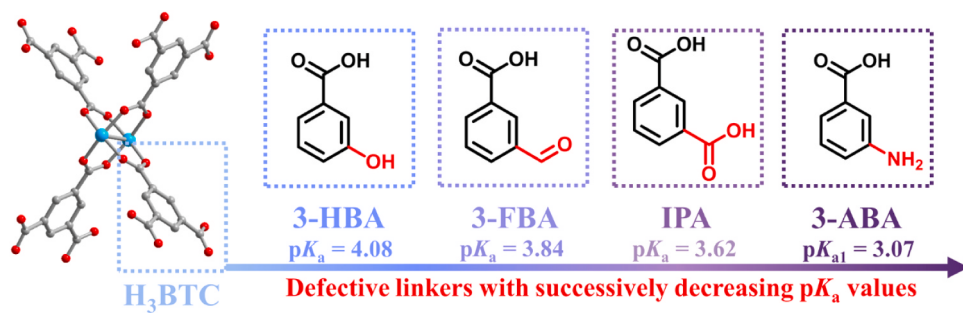
The electrochemical impedance spectroscopy (EIS) and transient photocurrent response were obtained in a standard three-electrode experimental system via a CHI760E electrochemical analyzer. 100 μL of 20 mg/mL catalyst was applied on the conductive surface of the prepared fluorinated tin oxide glass (FTO), and then used as the working electrode after drying. The saturated calomel electrode (SCE) was used as reference electrode and Pt plate as the counter electrode.

3. Results and Discussion

3.1. Synthesis and characterization of defective Cu-BTC with different defective linkers

In this work, a series of defective linkers (3-FBA = 3-Formylbenzoic acid, 3-HBA = 3-Hydroxybenzoic acid, 3-NBA = 3-Nitrobenzoic acid, 3-ABA = 3-Aminobenzoic acid, IPA = Isophthalic acid; Scheme 1) were systematically incorporate into Cu-BTC framework via the mixed-component approach. Compared with the bridging ligand H_3BTC , IPA acts as an auxiliary ligand has only two carboxylate sites. The other defective linkers contain a carboxyl group and varying functional groups present at the 3-position (3-FBA = -CHO, 3-HBA = -OH, 3-NBA = -NO₂, 3-ABA = -NH₂). Since the pK_a value directly affect the deprotonation and coordination ability of defective linkers, the defective linkers with successively decreasing pK_a value were selected to study the effects of different linkers on the defect degree and photocatalytic performance of Cu-BTC.

SEM images as shown in Fig. 1 reveal the influence of different defective linkers on the material morphology. Fig. 1a shows that pure Cu-BTC material has a typical octahedral structure. The morphology of the Cu-BTC-ABA sample (Fig. 1b) clearly changes from octahedral to irregular rectangular, which indicates that the addition of auxiliary ligand (3-ABA (-NH₂)) may adjust the coordination and crystal growth



Scheme 1. Regulation of Cu-BTC by incorporating different defective linkers with successively decreasing pK_a value. (The pK_a value of the defective linkers were obtained from LANGE'S HANDBOOK OF CHEMISTRY).

process of Cu-BTC. The Cu-BTC-FBA (Fig. 1c₁ and c₂) and Cu-BTC-HBA (Fig. 1d₁ and d₂) samples retain octahedral morphology of the parent Cu-BTC except that the detailed surfaces become rugged. The surface roughness may be due to the defect structure created by ligand substitution. When IPA was used as a defective linker, the crystal dimensions decrease obviously from ~20 μm to ~100 nm (Fig. 1e). The illustrations of different Cu-BTC variants are shown in Fig. 1f.

The powder XRD patterns of the pure Cu-BTC and Cu-BTC variants are shown in Fig. 2a and b. Cu-BTC-FBA, Cu-BTC-HBA and Cu-BTC-IPA have the typical Cu-BTC topological structure reported in the literature, which is also in agreement with the simulation pattern provided by the Materials Studio package 5.0 [19]. The results indicate that the topological structure of the above three variants does not change after the introduction of different defective linkers (3-FBA, 3-HBA and IPA). However, the characteristic peak of Cu-BTC-ABA is completely different from that of pure Cu-BTC, which indicates that the structure of Cu-BTC has been disrupted. In addition, the color of the crystal obtained after the introduction of 3-ABA is green, which is different from the color (blue) of Cu-BTC and other variant samples (Fig. S1). These phenomenon may be due to the preferential coordination of 3-ABA with Cu^{2+} during the formation of Cu-BTC. 3-ABA involved in the construction of crystal structure makes H₃BTC unable to effectively link with Cu^{2+} , leading to changes in the topologic structure. As shown in Fig. 2b, the subtle variations of Cu-BTC-FBA and Cu-BTC-IPA in the low-angle peak positions may be related to the ordered missing-cluster defects, as reported in the literature [16]. The results of SEM and XRD show that 3-ABA (-NH₂) with smaller pK_a will destroy the structure of Cu-BTC, thus, pure Cu-BTC, Cu-BTC-FBA, Cu-BTC-HBA and Cu-BTC-IPA were selected as samples for subsequent characterization and performance studies.

FT-IR spectra of all Cu-BTC samples are shown in Fig. S2. All Cu-BTC samples present the distinct FT-IR pattern with peaks located at 2500–3407, 1368, 721 and 488 cm^{-1} , which are consistent with literature reports [20,21]. The strong wideband at 2500–3407 cm^{-1} indicates the presence of carboxyl groups from H₃BTC in the Cu-BTC structure. Meanwhile, the absorption peak at 1368 cm^{-1} is associated with the stretching mode of C-O. Also, the bands locate at 721 and 488 cm^{-1} may be related to the bending mode and stretching mode of Cu-O, respectively. Cu-BTC variants maintain the typical band shape of pure Cu-BTC, indicating that the introduction of defective linkers does not destroy the topological structure of Cu-BTC. Meanwhile, the FT-IR spectra of Cu-BTC variants were compared with those of the corresponding defective linkers. Figs. S2b-d spectra show that the characteristic absorption peaks of defective linkers appear in the FT-IR spectra of the Cu-BTC variants, and new bands and band shifts were observed due to the doping of these defective linkers. The results confirm that the defective linkers are effectively incorporated into the structure of the corresponding variants without destroying the matrix structure of parent Cu-BTC. The effect of the introduction of different defective linkers on the thermal stability of Cu-BTC was studied via the variation of TG curves, as shown in Fig. S3. Compared with pure Cu-BTC, the TG characteristic curves of Cu-BTC variants have no significant change

except that the structure collapse temperatures shift to lower temperature in different degrees, and Cu-BTC-IPA sample shows the most obvious shift. In addition, the weight loss platform of the defective Cu-BTC sample was observed to be lower than that of the pure Cu-BTC sample. It may be due to the higher the number of missing linkers, the lower the percentage of linker masses relative to the total mass of the structure, and therefore the smaller the related weight loss plateau observed [22,23]. The results indicate that the overall thermal stability of Cu-BTC variants is lower than that of pure Cu-BTC, which may be due to the weak coordination between copper and the defective linker, and the absence of linkers.

3.2. Formation and structural analysis of defective Cu-BTC

To further verify whether the linkers participate in the construction of framework structure, the reaction process was monitored by UV-vis absorption spectra. As shown in Fig. S4a, the absorption peak of blue Cu (NO₃)₂.3 H₂O solution (solution a) is located at 205 nm. The absorption peak of the colorless H₃BTC solution appears at 212 nm (Fig. S4b), and the colorless 3-FBA solution appears at 216 nm (Fig. S4c). When H₃BTC was slowly added dropwise to the Cu(NO₃)₂.3 H₂O solution to form solution b, the characteristic peak of the mixed solution shifts to 209 nm. Because different substance and coordination compound have their characteristic absorption spectra, 3-FBA was dropped into the mixed solution of Cu²⁺ and H₃BTC to investigate the effect of defect on the coordination between H₃BTC and Cu²⁺ (Fig. S4d). After adding 3-FBA, the color of the mixed solution was still blue, but the absorption peak of the mixed solution shifts to 212 nm. The result confirm that the defective linker (3-FBA) can coordinate with Cu²⁺ in Cu-BTC structure by the competitive coordination with H₃BTC, thereby forming the defect structure and regulating the Cu CUS.

The N₂ adsorption-desorption isotherms and the pore size distribution of pure Cu-BTC and Cu-BTC variants are presented in Fig. 2c and d, respectively. The specific surface area of Cu-BTC variants is slightly increased than pure Cu-BTC, which may be caused by the introduction of vacancy and mesoporous in the framework [24]. The isotherms hysteresis loops observed in Cu-BTC variants are also attributed to the mesoporous structure [25,26]. Meanwhile, the pore size distribution of pure Cu-BTC and Cu-BTC variants also distinctly shows the presence of mesoporous structure in samples. Above results indicate that the specific surface area and mesoporous structure can be increased by introducing defective linkers into Cu-BTC structure, and the order of specific surface area of materials is: Cu-BTC-FBA (-CHO, 1709 $\text{m}^2 \cdot \text{g}^{-1}$) > Cu-BTC-HBA (-OH, 1532 $\text{m}^2 \cdot \text{g}^{-1}$) > Cu-BTC-IPA (-COOH, 993 $\text{m}^2 \cdot \text{g}^{-1}$) > Cu-BTC (897 $\text{m}^2 \cdot \text{g}^{-1}$). Although the specific surface area of Cu-BTC-HBA increases, the mesoporous structure does not change significantly. In contrast, Cu-BTC-IPA exhibits the least improve in specific surface area but a more obvious increase in mesoporous distribution at 25–50 nm, which may be due to the presence of larger apertures in the structure will reduce the specific surface area. The specific surface area of Cu-BTC-FBA is the largest and the mesoporous distribution at 5–10 nm

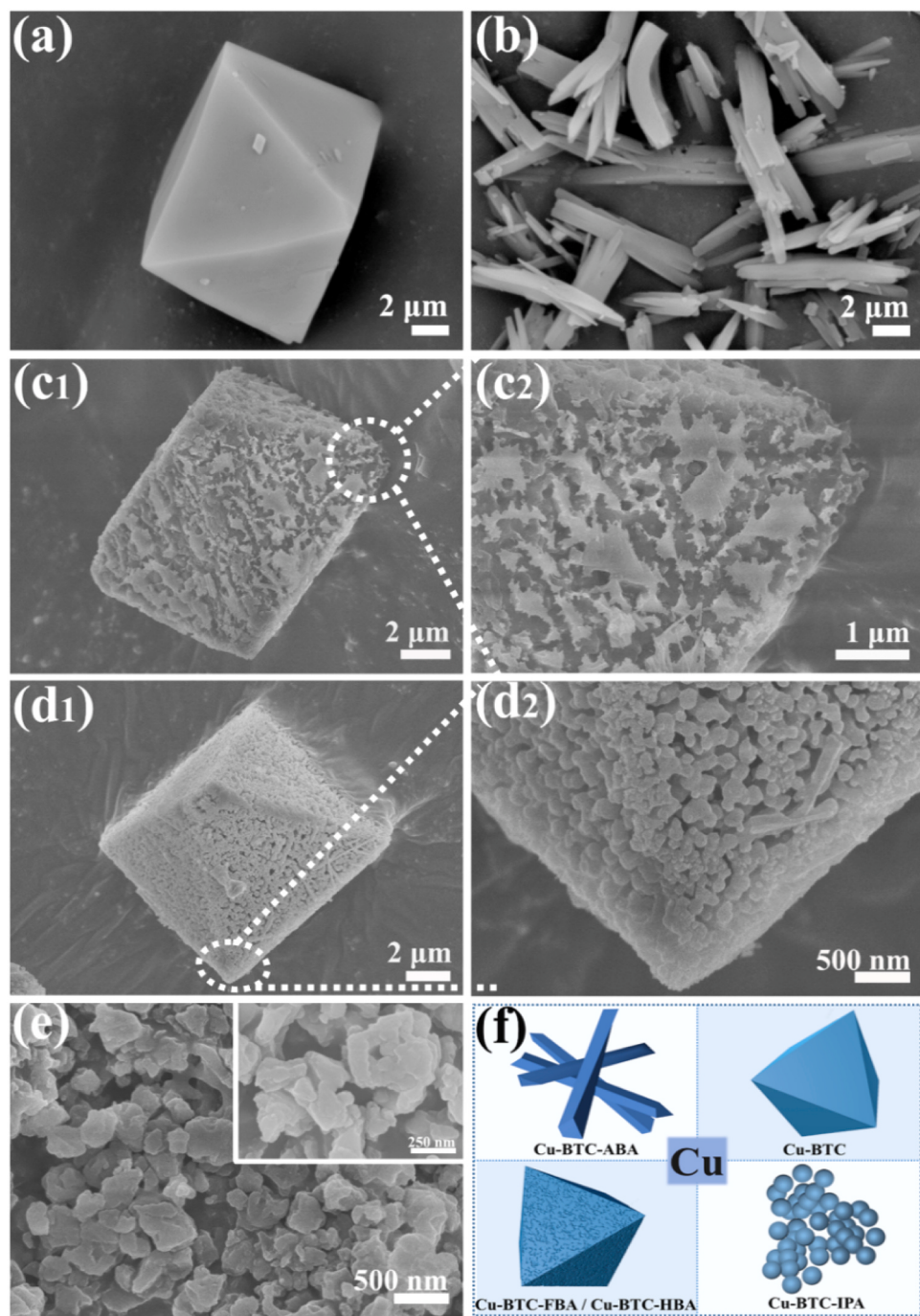


Fig. 1. The SEM images of the samples: (a) Cu-BTC; (b) Cu-BTC-ABA (-NH₂); (c₁₋₂) Cu-BTC-FBA (-CHO); (d₁₋₂) Cu-BTC-HBA (-OH); (e) Cu-BTC-IPA (-COOH); (f) schematic diagrams of different Cu-BTC samples.

increased significantly, which is beneficial to the exposure of active sites and the transport of guest molecules.

The defect concentration in the photocatalyst has a crucial effect on the photocatalytic activity of the material, and the pK_a value of the defective linkers can regulate the defect concentration by affecting the deprotonation rate of the linkers. Therefore, the formation mechanism of defect structure and mixed-valence state in Cu-BTC was investigated, which is conducive to the design and synthesis of defective MOFs with moderate defect concentration.

The proposed strategy for preparing defective Cu-BTC materials via introducing defective linkers is shown in Fig. 3a. In pure Cu-BTC framework structure, H₃BTC coordinates with Cu²⁺ to form Cu²⁺

CUS after deprotonation. The defective linkers (3-FBA, 3-HBA, or IPA) as the auxiliary ligands are incorporated into Cu-BTC framework to form the defect structure by competing with the original ligand and coordinating with Cu²⁺. Compared with H₃BTC, the IPA has one less carboxylic acid group, and the aldehyde group (-CHO) and hydroxyl group (-OH) at the end of the 3-FBA and 3-HBA molecules cannot bridge the surrounding copper cations, which results in the formation of vacancies in Cu-BTC structure. Moreover, the introduction of defective linkers leads to the formation of Cu¹⁺ sites in structure because of the charge compensation. These results indicate that the electronic property (metal valance) and steric property (ligand vacancy) at Cu CUS in MOFs structure can be regulated simultaneously via the introduction of

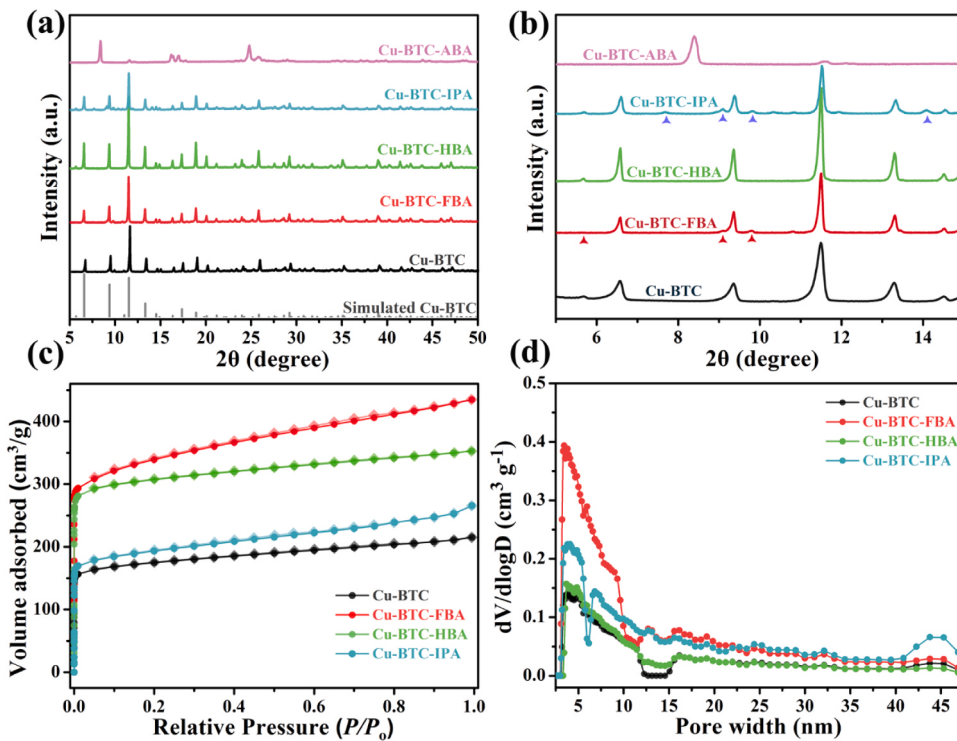


Fig. 2. (a) PXRD pattern with peaks located at 5–50°; (b) PXRD pattern with peaks located at 5–15°; (c) N₂ adsorption/desorption isotherms of Cu-BTC and Cu-BTC variants; (d) Pore size distributions of Cu-BTC and Cu-BTC variants.

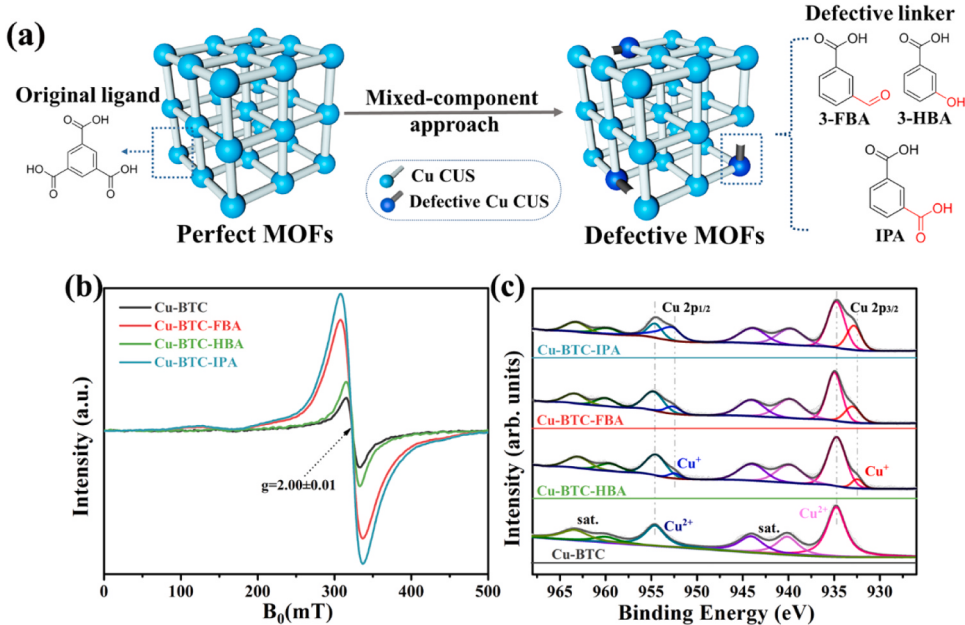


Fig. 3. (a) The schematic diagram for the structure of Cu-BTC and defective Cu-BTC synthesized by introducing the defective linkers via mixed-component approach; (b) EPR spectra of Cu-BTC and Cu-BTC variants; (c) Co 2p XPS peaks of Cu-BTC and Cu-BTC variants.

defective linkers.

3.3. Ligand vacancies and Cu¹⁺/Cu²⁺ CUss in defective Cu-BTC

In order to verify the above proposed mechanism, the EPR spectra were tested to monitor the behaviors of trapped electrons and surface vacancies. The EPR results (Fig. 3b) show that the pure Cu-BTC sample also has EPR signal, suggesting the presence of some intrinsic defects in

Cu-BTC framework due to misconnections/dislocations during the crystallization or activation process [27,28]. Compared with pure Cu-BTC, Cu-BTC variants exhibit stronger EPR signal, indicating that the insertion of defective linkers can partially replace the original ligand to form structural defects. The order of defect concentration of samples is Cu-BTC-IPA (-COOH) > Cu-BTC-FBA (-CHO) > Cu-BTC-HBA (-OH) > Cu-BTC.

Relevant literatures and our previous work found that the

introduction of auxiliary ligand into MOFs framework can not only form defect structure, but also regulate the metal valence state to form mixed-valence CUS [17,29]. It is confirmed by the density of states (DOS) that the removal of linker can lead to a change in the metal atom environment, which tends to reduce unoccupied orbitals (δ ELMCT) and increase charge transfer, thus improving the photocatalytic activity [30]. Notably, electronic modification on CUS could overcome the limited active site specificity and endow materials with special reactivity properties [31]. Meanwhile, the mixed-valence structure can significantly enhance the separation rate of photogenerated electron-hole pairs and suppress their recombination [32].

The removal of ligands is accompanied with the charge compensation of the node, which is usually achieved by the change of metal valence state. Thus, the XPS analysis can provide direct spectroscopic evidence for the change of electronic state of copper species in defective Cu-BTC material. The C 1 s XPS spectra of samples are divided into three peaks at 288.6 eV, 286.4 eV and 284.8 eV, which are identified as -COO, C-H/C-OH and C-C, respectively (Fig. S5) [33,34]. Besides, the O 1 s region (Fig. S6) shows two characteristic peaks with binding energy of 533.6 eV and 531.7 eV, corresponding to H₂O and -COO/C-OH, respectively [35]. The Cu 2p XPS spectrum is shown in Fig. 3c, pure Cu-BTC shows two strong diffraction peaks of Cu²⁺ at 934.7 eV and 954.5 eV, corresponding to Cu 2p_{3/2} and Cu 2p_{1/2}, respectively [36,37]. Meanwhile, the shakeup satellite peaks situated at 962.5 eV and 942.9 eV, respectively, indicate the presence of Cu²⁺ species [38]. Compared with pure Cu-BTC, the XPS spectra of Cu 2p_{3/2} and Cu 2p_{1/2} in the Cu-BTC variants split the characteristic peaks of low-valence copper (Cu¹⁺) at 933.1 and 953.1 eV, respectively [37,39]. It suggests that some Cu²⁺ in CUS can be reduced to Cu¹⁺ after introduction of the

defective linkers. The possible reasons for the formation of Cu¹⁺ are charge compensation caused by ligand missing on Cu CUS [40], and its contents may be correlate with the defect numbers. The result indicates that the electronic property (metal valence) and spatial property (linker vacancy) of Cu CUS can be adjusted simultaneously by combining defective linkers into Cu-BTC framework, and the contents of Cu¹⁺ are proportional to defects. The order of Cu¹⁺ contents in different Cu-BTC variants is Cu-BTC-IPA (-COOH) > Cu-BTC-FBA (-CHO) > Cu-BTC-HBA (-OH), which is consistent with defect concentration.

As shown in Fig. 4, the pK_a value of the defective linker is correlated with the contents of defect structure and Cu¹⁺/Cu²⁺ CUS in Cu-BTC framework. It should be specifically noted that the pK_a value of the defective linker should not be too low to avoid the preferential coordination of metal ions with the defective linker, leading to the destruction of MOFs structure. The literatures pointed out that the modulator with a small pK_a generally provides high defect concentration [41,42]. This may be due to the modulator with lower pK_a can readily replace the original ligand, and the incomplete exchange will cause structural defects [43]. Theoretically, the lower pK_a value of the defective linker, the more defect and Cu¹⁺/Cu²⁺ CUS contents can be produced in the formed Cu-BTC variant. According to the XPS and EPR results, the order of defect and Cu¹⁺/Cu²⁺ CUS contents of a series of Cu-BTC variants is: Cu-BTC-IPA (-COOH) > Cu-BTC-FBA (-CHO) > Cu-BTC-HBA (-OH). The pK_a value of defective linkers are IPA (3.62) < 3-FBA (3.84) < 3-HBA (4.08) in order. It indicates that the pK_a value of auxiliary ligands are negatively associated with the contents of defect structure and mixed-valence states in MOFs framework.

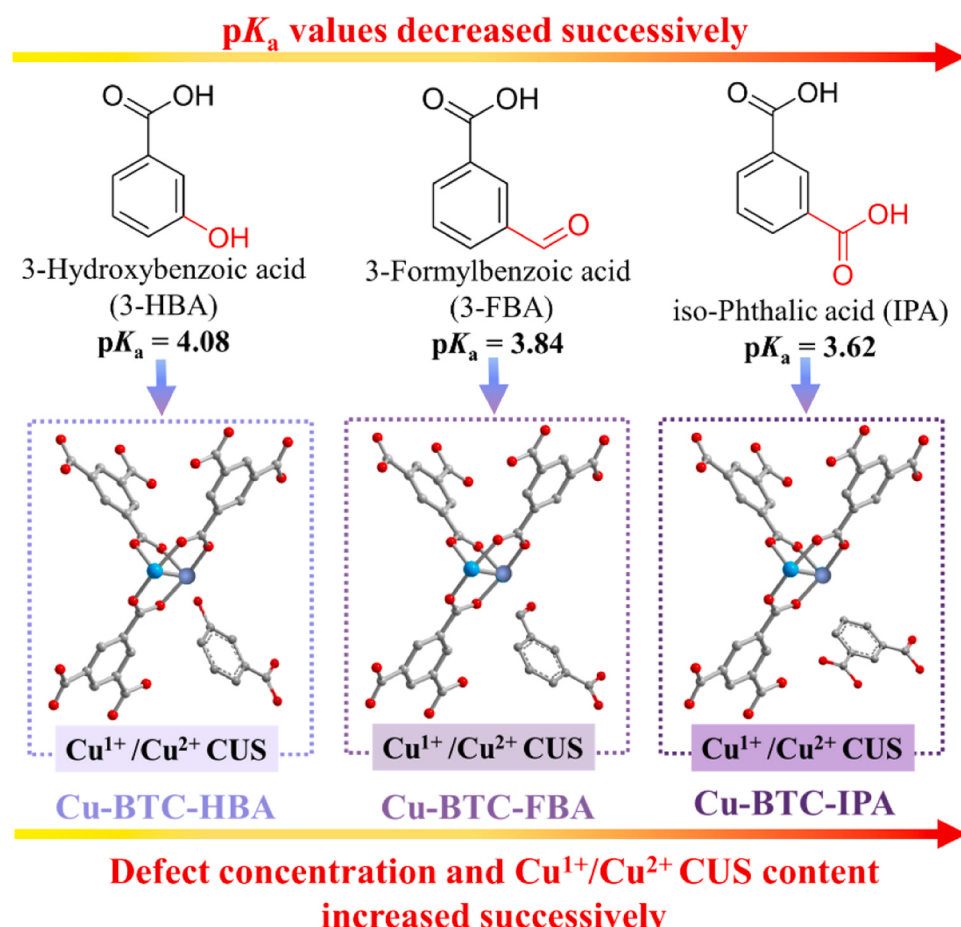


Fig. 4. Relationship between pK_a value of defective linkers and the contents of defect and Cu¹⁺/Cu²⁺ CUS in Cu-BTC framework.

3.4. Photocatalytic performance of defective Cu-BTC

As is well known, defect structure in photocatalyst can regulate the light absorption behavior and tailor the bandgap. In photocatalytic reactions, the defect structure can also regulate the electronic structure and property of light-excited carriers by introducing additional energy levels [44]. The mixed-valence structure also can improve the separation and transfer rate of photogenerated electron-hole pairs. Based on these factors, defective Cu-BTC with mixed-valence states will exhibit outstanding photocatalytic performance. To further verify the influence of defective linkers on the photocatalytic performance of Cu-BTC variants, the water oxidation and water reduction properties of them were measured in different reaction systems (Fig. 5a and b).

Cu-BTC variants show the excellent bifunctional photocatalytic properties for H₂ evolution and O₂ evolution in water splitting reaction compared to pure Cu-BTC. The photocatalytic O₂ evolution rate of samples is sorted as follows: Cu-BTC-FBA (-CHO) 3942 μmol·g⁻¹·h⁻¹ > Cu-BTC-IPA (-COOH) 3037 μmol·g⁻¹·h⁻¹ > Cu-BTC-HBA (-OH) 2508 μmol·g⁻¹·h⁻¹ > Cu-BTC 1873 μmol·g⁻¹·h⁻¹, and the photocatalytic H₂ evolution rate of samples is sorted as follows: Cu-BTC-FBA (-CHO) 15107 μmol·g⁻¹·h⁻¹ > Cu-BTC-IPA (-COOH) 10171 μmol·g⁻¹·h⁻¹ > Cu-BTC-HBA (-OH) 9805 μmol·g⁻¹·h⁻¹ > Cu-BTC 7714 μmol·g⁻¹·h⁻¹. Cu-BTC-ABA has almost no photocatalytic activity of water oxidation, and H₂ generation rate for seven hours is lower than that of pure Cu-BTC. This may be due to the fact that the introduction of 3-ABA (-NH₂) can disrupt Cu-BTC structure. To determine the optimal reaction conditions, the

effect of different parameters in photocatalytic water oxidation/reduction reactions were systematically investigated (listed in Table S1 and Table S2). Cu-BTC-FBA shows the best photocatalytic performance, with O₂ and H₂ generation rates of 3942 μmol·g⁻¹·h⁻¹ (2.10 times than that of Cu-BTC) and 15107 μmol·g⁻¹·h⁻¹ (1.94 times than that of Cu-BTC), respectively. Most of the Cu-based photocatalysts reported in the literatures can only catalyze water oxidation to produce oxygen or water reduction to produce hydrogen. Although some Cu-based photocatalysts can act as bifunctional catalysts to catalyze overall water decomposition, expensive Ru-based photosensitizers are usually required, and the yields of oxygen and hydrogen are relatively lower. Compared with reported Cu-based photocatalysts, the prepared noble-free Cu-BTC variants are efficient bifunctional photocatalyst for water oxidation and water reduction reactions, as shown in Table S3.

Stability is one of the important factors for catalysts. To study the stability of the defective Cu-BTC photocatalysts, the optimal photocatalyst (Cu-BTC-FBA) was selected for recycling experiments (Fig.S7a and Fig.S7b). After five cycles, the photocatalytic performance does not decrease significantly, indicating that Cu-BTC-FBA has good recyclability. By comparing the XRD spectra of Cu-BTC-FBA before and after the water oxidation reaction (Fig.S7c and Fig.S7d), it was found that the material is transformed to CuO (PDF#89-5898) in the photocatalytic water oxidation system. However, in the photocatalytic water reduction system, the structure of the Cu-BTC-FBA does not change significantly before and after the recycling experiments. This phenomenon may be due to the fact that the structure of MOFs is prone to decomposition

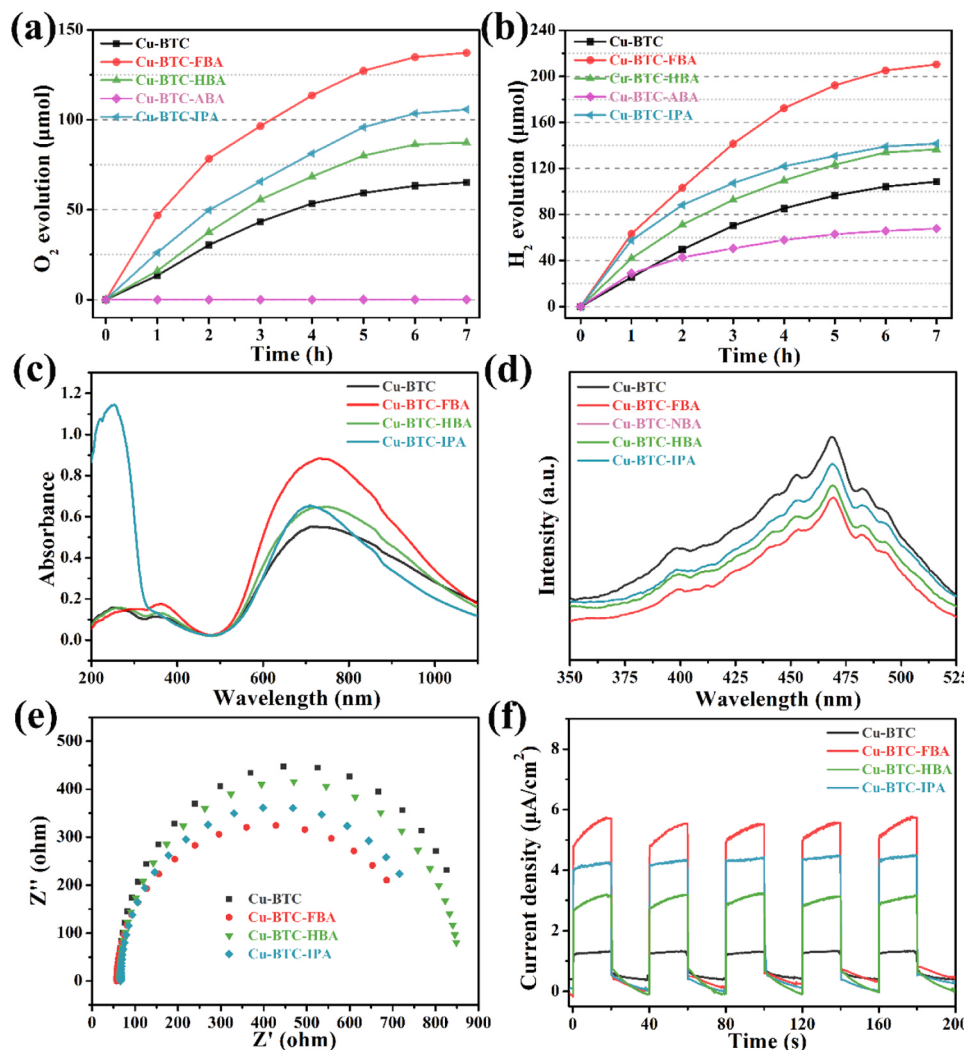


Fig. 5. (a) Time-dependent O₂ production over pure Cu-BTC and Cu-BTC variants under the photocatalytic water oxidation system; (b) Time-dependent H₂ production over pure Cu-BTC and Cu-BTC variants under the photocatalytic water reduction system; (c) UV-vis diffuses reflectance spectra (DRS) of Cu-BTC and defective Cu-BTC samples; (d) Photoluminescence spectra (PL) performance; (e) Nyquist diagrams of electrochemical impedance spectroscopy; (f) Transient photocurrent response.

under alkaline conditions (water oxidation system). Therefore, the design and synthesis of acid- and base-resistant and water-stable MOFs materials is the focus of further research.

3.5. Mechanism and photocatalytic activity trend of defective Cu-BTC

To study the effect of defect structure on the light absorption capacity and the separation efficiency of charge carriers, UV-vis DRS and PL were systematically studied. Compared with pure Cu-BTC, the defective Cu-BTC samples show higher absorption strength and broader optical absorption range, indicating that the defect structure can significantly enhance the visible light absorptivity of defective Cu-BTC (Fig. 5c) [45,46]. To verify this conclusion, wavelength-dependent photocatalytic water oxidation reaction were tested. It can be seen from Fig. S8, Cu-BTC-FBA has better photocatalytic water oxidation performance than Cu-BTC under different wavelengths. This result indicates that the light absorption capacity of Cu-BTC-FBA can be extensively improved by the defective structure, which is consistent with that of solid-state UV.

It can be found from the UV-vis DRS spectra that the light absorption performance of Cu-BTC-FBA is better than that of other samples, which is consistent with photocatalytic activity. Meanwhile, defects can lead to the new energy levels to tailor bandgap, and the photocatalysts with narrow bandgap energy have greater advantages in photocatalytic applications. Thus, the bandgap energies of all samples are shown in Fig. S9, and the bandgap energy (E_g) of Cu-BTC, Cu-BTC-FBA, Cu-BTC-HBA and Cu-BTC-IPA were determined to be 2.62, 2.41, 2.64 and 3.75 eV, respectively. These results indicate that Cu-BTC-FBA has the most suitable defect concentration, which can effectively improve the light absorption capacity and narrow the bandgap. Most of the light absorption and subsequent photoexcitation occurs on the surface of photocatalysts [47], so, the PL signal can reflect the separation efficiency of photogenerated electron-hole pairs. The smaller PL signal indicates that the carrier separation efficiency is lower, and thus the photogenerated electrons and holes cannot be effectively used to enhance catalytic activity. As shown in Fig. 5d, the intensity order of the PL spectrum is as follows: Cu-BTC > Cu-BTC-HBA (-OH) > Cu-BTC-IPA (-COOH) > Cu-BTC-FBA (-CHO), suggesting that the defect structure can effectively inhibit the recombination of electrons and holes. Meanwhile, the Cu-BTC-FBA sample shows the lowest PL signal, which implies that the activity time of electrons and holes is the longest. The higher PL signal of Cu-BTC-IPA compared to Cu-BTC-FBA may be due to the excessive defects can act as electron-hole recombination sites, which can decrease the lifetime of photo-generated electrons and holes.

The electrochemical impedance spectroscopy (EIS) and the transient photocurrent response were tested in Fig. 5e and Fig. 5f to further explore the charge transfer behavior and separation efficiency. The interface charge transport behavior of samples was studied by the Nyquist plots, the smaller radius of arc means a lower transfer resistance. The charge-transfer resistance of all defective Cu-BTC samples is lower than that of pure Cu-BTC, suggesting that the defect structure is conducive to electrons transfer. Compared with other defective Cu-BTC samples, Cu-BTC-FBA has the lowest charge transfer resistance, which indicates that its interfacial charge transfer rate is the fastest in all samples. During on/off irradiation cycles under visible-light, the photocurrent density of Cu-BTC-FBA is higher than that of other samples, implying that it has higher light utilization and more efficient electron transfer rate.

The different properties of defective Cu-BTC samples described in this paper were summarized in Fig. 6 to fully understand the influence of the pK_a value on the MOFs properties. It can be found that defect and Cu^{1+}/Cu^{2+} CUS content in the synthesized defective Cu-BTC structure are inversely proportional to the pK_a value of defective linkers. This indicates that the introduction of defective linkers with lower pK_a value facilitates the formation of MOFs photocatalysts with higher defect and Cu^{1+}/Cu^{2+} CUS content. In addition, the increase of defects and mixed

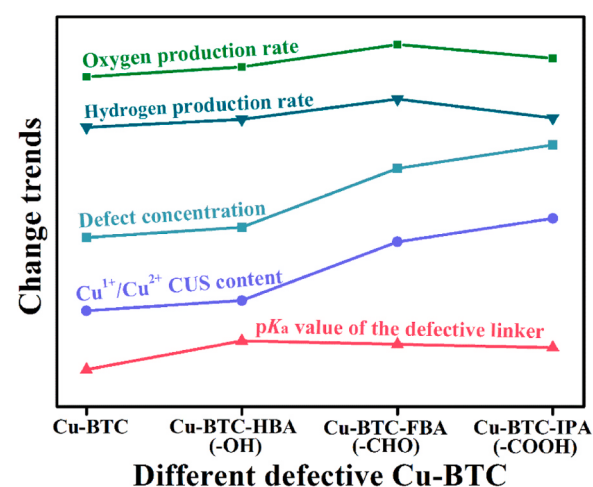


Fig. 6. The different properties variation trends of defective Cu-BTC samples.

valence content can improve the performance of photocatalytic hydrogen and oxygen evolution, but excessive defects will reduce the catalytic activity as a recombination sites. Therefore, in the subsequent design of photocatalysts, defect ligand with appropriate pK_a value should be selected to obtain excellent photocatalysts.

Based on above results, the possible mechanism of photocatalytic water oxidation reaction over the defective Cu-BTC was illustrated in Fig. 7a. Under visible light irradiation, the defective Cu-BTC is excited to produce electron-hole ($e^- - h^+$) pairs. The $e^- - h^+$ pairs can rapidly separate into single electrons and holes to transfer to the LUMO and HOMO orbitals, respectively. The photogenerated electrons on the LUMO orbital reduce $S_2O_8^{2-}$ to SO_4^{2-} in solution, while the photogenerated holes gathered on the HOMO orbital oxidize water to produce oxygen. [48]. The speculated mechanism of the photocatalytic H_2 production by water reduction reaction in EY-sensitized system was illustrated in Fig. 7b. The defective Cu-BTC is excited by absorbing photons under visible-light irradiation, and then electrons move to LUMO orbital and holes move to HOMO orbital. The EY absorb photons to generate excited state EY^{1*} under visible light, and the EY^{1*} rapidly form the lowest-lying triplet excited state EY^{3*} by the intersystem crossing (ISC) progress. EY^{3*} is further quenched to form EY^{\bullet} , and electron move from EY^{\bullet} to defective Cu-BTC [49]. The photogenerated electrons on the LUMO orbital continue to react with the proton in solution to form H_2 .

In photocatalytic reactions, the defects with different concentration present in the form of shallow or deep trapped states [50]. Low concentration defects appear preferentially on the crystal surface and form the shallow states. The electrons captured by the shallow states are easily trapped back to the LUMO orbital, which can increase the carrier density and improve the photocatalytic activity of materials. However, the high concentration defects make it easier for electrons and holes to enter the catalyst structure and form deep states. The electrons trapped by the deep states are immobilized and difficult to migrate back to the LUMO orbital. These electrons will combine with the holes to cause serious recombination of carriers. It is found that the high concentration defects in Cu-BTC-IPA sample can act as recombination centers to shorten the lifetime of electrons and holes, and reduce the photocatalytic performance of material. Thus, controlling the defect content in the structure is an important factor to improve the photocatalytic activity.

4. Conclusions

In summary, three defective Cu-BTC bifunctional photocatalysts were successfully synthesized via introducing defective linkers with different pK_a value. The defective linkers can create defects in Cu-BTC framework by the competitive coordination. Meanwhile, Cu^{2+}/Cu^{2+}

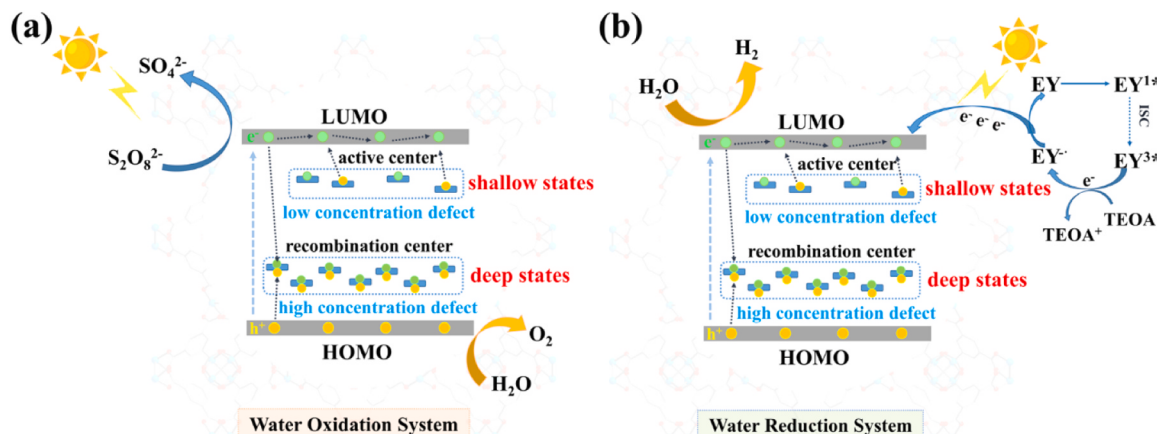


Fig. 7. (a) The proposed photocatalytic mechanism for oxygen evolution in different system under visible light irradiation; (b) The proposed photocatalytic mechanism for hydrogen evolution in different system under visible light irradiation.

CUS can partially transformed into $\text{Cu}^{1+}/\text{Cu}^{2+}$ CUS via the charge compensation. It is found that the defective linkers with lower pK_a value would create more defect and $\text{Cu}^{1+}/\text{Cu}^{2+}$ in the Cu-BTC structure. While, when the pK_a value is too low, the crystal structure of Cu-BTC will be destroyed. Furthermore, the defective structures and mixed $\text{Cu}^{1+}/\text{Cu}^{2+}$ CUS can regulate the pore structure, improve the light absorption capacity, accelerate the separation/transfer efficiency of electrons and holes, and act as the active sites for photocatalytic reaction. Cu-BTC-FBA has the best photocatalytic overall water decomposition performance because of its suitable defect concentration and the largest specific surface area. The performance of Cu-BTC-IPA with the largest defect concentration is not optimal catalyst since too many defects may serve as the recombination centers to reduce its photocatalytic activity. This study provides some ideas for the selection of defective linkers with different functional groups and pK_a value to construct defective MOFs with improved structure and electronic properties. The prepared defective MOFs can not only be used for photocatalytic water splitting, but also can be further expanded to photocatalytic degradation and oxidation of organic substances.

CRediT authorship contribution statement

Sample CRediT author statement. Li Zhang: performed the experimental work, wrote the manuscript. Changyan Guo: conceived and oversaw the project, jointly wrote the manuscript. Tingxiang Chen: performed part experimental work. Yuan Guo: suggested experiments. Afaq Hassan: polished the writing. Yuli Kou: analyzed data. Cheng Guo: performed part tests. Jide Wang: conceived and oversaw the project.

Declaration of Competing Interest

The authors declare that they have no known competing financial interests or personal relationships that could have appeared to influence the work reported in this paper.

Acknowledgements

This work was supported by the Doctoral Scientific Research Foundation of Xinjiang University (No. 620320012); the National Natural Science Foundation of China (No. 22169018; No. 21861035); the Natural Science Foundation of Xinjiang Uyghur Autonomous Region (2021D01C091).

Appendix A. Supporting information

Supplementary data associated with this article can be found in the

online version at doi:10.1016/j.apcatb.2021.120888.

References

- [1] M.K.H. Rabaia, M.A. Abdelkareem, E.T. Sayed, K. Elsaid, K. Chae, T. Wilberforce, A.G. Olabi, Environmental Impacts of Solar Energy Systems: A Review, *Sci. Total Environ.* 754 (2021), 141989.
- [2] Y. Li, K. Wang, D. Huang, L. Li, J. Tao, N.A.A. Ghany, F. Jiang, $\text{Cd}_x\text{Zn}_{1-x}\text{S}/\text{Sb}_2\text{Se}_3$ Thin Film Photocathode for Efficient Solar Water Splitting, *Appl. Catal. B: Environ.* 286 (2021), 119872.
- [3] A. Melillo, M. CabreroAntonino, S. Navalón, M. Álvaro, B. Ferrer, H. García, Enhancing Visible-light Photocatalytic Activity for Overall Water Splitting in $\text{UiO}-66$ by Controlling Metal Node Composition, *Appl. Catal. B: Environ.* 278 (2020), 119345.
- [4] H. Hu, Z. Wang, L. Cao, L. Zeng, C. Zhang, W. Lin, C. Wang, Metal-Organic Frameworks Embedded in a Liposome Facilitate Overall Photocatalytic Water Splitting, *Nat. Chem.* 13 (2021) 358–366.
- [5] T. Toyao, M. Saito, Y. Horiuchi, K. Mochizuki, M. Iwata, H. Higashimura, M. Matsuoka, Efficient Hydrogen Production and Photocatalytic Reduction of Nitrobenzene over a Visible-Light-Responsive Metal-Organic Framework Photocatalyst, *Catal. Sci. Technol.* 3 (2013) 2092–2097.
- [6] Y. Horiuchi, T. Toyao, M. Saito, K. Mochizuki, M. Iwata, H. Higashimura, M. Anpo, M. Matsuoka, Visible-Light-Promoted Photocatalytic Hydrogen Production by Using an Amino-Functionalized Ti(IV) Metal-Organic Framework, *J. Phys. Chem. C* 116 (2012) 20848–20853.
- [7] W. Wang, X. Xu, W. Zhou, Z. Shao, Recent Progress in Metal-Organic Frameworks for Applications in Electrocatalytic and Photocatalytic Water Splitting, *Adv. Sci.* 4 (2017), 1600371.
- [8] L. Shi, D. Benetti, F. Li, Q. Wei, F. Rosei, Phase-junction Design of MOF-derived TiO_2 Photoanodes Sensitized with Quantum Dots for Efficient Hydrogen Generation, *Appl. Catal. B: Environ.* 263 (2020), 118317.
- [9] X. Liu, S. Chen, S. Li, H. Nie, Y. Feng, Y. Fan, M. Yu, Z. Chang, X. Bu, Structural Tuning of Zn(II)-MOFs Based on Pyrazole-Functionalized Carboxylic Acid Ligands for Organic Dye Adsorption, *CrystEngComm* 22 (2020) 5941–5945.
- [10] S. Dissegna, K. Epp, W.R. Heinz, G. Kieslich, R.A. Fischer, Defective Metal-Organic Frameworks, *Adv. Mater.* 30 (2018), 1704501.
- [11] C. Schneider, M. Mendt, A. Poppl, V. Crocella, R.A. Fischer, Scrutinizing the Pore Chemistry and the Importance of Cu(I) Defects in TCNQ-Loaded $\text{Cu}_3(\text{BTC})_2$ by a Multitechnique Spectroscopic Approach, *ACS Appl. Mater. Inter.* 12 (2019) 1024–1035.
- [12] D. Maarisetty, S.S. Baral, Defect Engineering in Photocatalysis: Formation, Chemistry, Optoelectronics, and Interface Studies, *J. Mater. Chem. A* 8 (2020) 18560–18604.
- [13] R. Qi, P. Yu, J. Zhang, W. Guo, Y. He, H. Hojo, H. Einaga, Q. Zhang, X. Liu, Z. Jiang, W. Shangguan, Efficient Visible Light Photocatalysis Enabled by the Interaction between Dual Cooperative Defect Sites, *Appl. Catal. B: Environ.* 274 (2020), 119099.
- [14] O. Kozačuk, I. Luz, F.X. Llabres, i Xamena, H. Noei, M. Kauer, H.B. Albada, E.D. Bloch, B. Marler, Y. Wang, M. Muhler, Multifunctional, Defect-Engineered Metal-Organic Frameworks with Ruthenium Centers: Sorption and Catalytic Properties, *Angew. Chem. Int. Ed.* 53 (2014) 7058–7062.
- [15] D. Wu, W. Yan, H. Xu, E. Zhang, Q. Li, Defect Engineering of Mn-based MOFs with Rod-shaped Building Units by Organic Linker Fragmentation, *Inorg. Chim. Acta* 460 (2017) 93–98.
- [16] N. Assaad, G. Sabeh, M. Hmadeh, Defect Control in Zr-Based Metal-Organic Framework Nanoparticles for Arsenic Removal from Water, *ACS Appl. Nano Mater.* 3 (2020) 8997–9008.
- [17] Y. Guo, C. Feng, S. Wang, Y. Xie, C. Guo, Z. Liu, N. Akram, Y. Zhang, Y. Zhao, J. Wang, Construction of Planar-type Defect-Engineered Metal-Organic

Frameworks with both Mixed-valence Sites and Copper-ion Vacancies for Photocatalysis, *J. Mater. Chem. A* 8 (2020) 24477–24485.

[18] H. Chen, L. Wang, J. Yang, R.T. Yang, Investigation on Hydrogenation of Metal-Organic Frameworks HKUST-1, MIL-53, and ZIF-8 by Hydrogen Spillover, *J. Phys. Chem. C* 117 (2013) 7565–7576.

[19] Y. Li, R.T. Yang, Hydrogen Storage in Metal-Organic and Covalent-Organic Frameworks by Spillover, *AIChE J.* 54 (2008) 269–279.

[20] S. Liu, L. Fu, Y. Liu, L. Meng, Y. Dong, Y. Li, M. Ma, Cu/C or Cu₂O/C Composites: Selective Synthesis, Characterization, and Applications in Water Treatment, *Sci. Adv. Mater.* 8 (2016) 2045–2053.

[21] F.N. Azad, M. Ghaedi, K. Dashtian, S. Hajati, V. Pezeshkpour, Ultrasonically Assisted Hydrothermal Synthesis of Activated Carbon-HKUST-1-MOF Hybrid for Efficient Simultaneous Ultrasound-assisted Removal of Ternary Organic Dyes and Antibacterial Investigation: Taguchi Optimization, Ultrasound. Sonochem. 31 (2016) 383–393.

[22] G.C. Shearer, S. Chavan, J. Ethiraj, J.G. Vitillo, S. Svelle, U. Olsbye, C. Lamberti, S. Bordiga, K.P. Lillerud, Tuned to Perfection: Ironing Out the Defects in Metal-Organic Framework UiO-66, *Chem. Mater.* 26 (2014) 4068–4071.

[23] M. Sun, J. Tie, G. Cheng, T. Lin, S. Peng, F. Deng, F. Ye, L. Yu, In Situ Growth of Burl-like Nickel Cobalt Sulfide on Carbon Fibers as High-performance Supercapacitors, *J. Mater. Chem. A* 3 (2015) 1730–1736.

[24] J.M. Taylor, S. Dekura, R. Ikeda, H. Kitagawa, Defect Control to Enhance Proton Conductivity in a Metal-Organic Framework, *Chem. Mater.* 27 (2015) 2286–2289.

[25] P.J. Branton, P.G. Hall, K.S.W. Sing, H. Reichert, F. Schüth, K.K. Unger, Physisorption of Argon, Nitrogen and Oxygen by MCM-41, a Model Mesoporous Adsorbent, *J. Chem. Soc., Faraday Trans.* 90 (1994) 2965–2967.

[26] P.C. Ball, R. Evans, Temperature Dependence of Gas Adsorption on a Mesoporous Solid: Capillary Criticality and Hysteresis, *Langmuir* 5 (1989) 714–723.

[27] W. Liang, C.J. Coglan, F. Ragon, M. Rubio-Martinez, D.M. D'Alessandro, R. Babarao, Defect Engineering of UiO-66 for CO₂ and H₂O Uptake - A Combined Experimental and Simulation Study, *Dalton T.* 45 (2016) 4496–4500.

[28] F. Ragon, P. Horcajada, H. Chevreau, Y.K. Hwang, U. Lee, S.R. Miller, T. Devic, J. Chang, C. Serre, In Situ Energy-Dispersive X-ray Diffraction for the Synthesis Optimization and Scale-up of the Porous Zirconium Terephthalate UiO-66, *Inorg. Chem.* 53 (2014) 2491–2500.

[29] W. Zhang, M. Kauer, P. Guo, S. Kunze, S. Cwik, M. Muhler, Y. Wang, K. Epp, G. Kieslich, R.A. Fischer, Impact of Synthesis Parameters on the Formation of Defects in HKUST-1, *Eur. J. Inorg. Chem.* 2017 (2017) 925–931.

[30] A. De Vos, K. Hendrickx, P. Van Der Voort, V. Van Speybroeck, K. Lejaeghere, Missing Linkers: An Alternative Pathway to UiO-66 Electronic Structure Engineering, *Chem. Mater.* 29 (2017) 3006–3019.

[31] J. He, Y. Xu, P. Shao, L. Yang, Y. Sun, Y. Yang, F. Cui, W. Wang, Modulation of Coordinative Unsaturation Degree and Valence State for Cerium-based Adsorbent to Boost Phosphate Adsorption, *Chem. Eng. J.* 394 (2020), 124912.

[32] Y. Guo, C. Feng, S. Qiao, S. Wang, T. Chen, L. Zhang, Y. Zhao, J. Wang, Magnetic Fe₃O₄-encapsulated VAN@MIL-101(Fe) with Mixed-valence Sites and Mesoporous Structures as Efficient Bifunctional Water Splitting Photocatalysts, *Nanoscale* 12 (2020) 12551–12560.

[33] N.A. Travlou, K. Singh, E. Rodríguez-Castellón, T.J. Bandosz, Cu-B.T.C. MOF-graphene-based, Hybrid Materials as Low Concentration Ammonia Sensors, *J. Mater. Chem. A* 3 (2015) 11417–11429.

[34] J. Du, C. Zhang, H. Pu, Y. Li, S. Jin, L. Tan, C. Zhou, L. Dong, HKUST-1 MOFs Decorated 3D Copper Foam with Superhydrophobicity/Superoleophilicity for Durable Oil/Water Separation, *Colloid Surf. A* 573 (2019) 222–229.

[35] Z. Fang, J.P. Dürholt, M. Kauer, W. Zhang, C. Lochenie, B. Jee, B. Albada, N. Metzler-Nolte, A. Pöppl, B. Weber, M. Muhler, Y. Wang, R. Schmid, R.A. Fischer, Structural Complexity in Metal-Organic Frameworks: Simultaneous Modification of Open Metal Sites and Hierarchical Porosity by Systematic Doping with Defective Linkers, *J. Mater. Chem. A* 136 (2014) 9627–9636.

[36] H. Zhang, Y. Muhammad, X. Cui, Z. Zhang, L. Liu, Z. Chu, J. Li, Y. Zhang, S.J. Shah, Z. Zhao, Engineering Bidirectional CMC-foam-supported HKUST-1@Graphdiyne with Enhanced Heat/Mass Transfer for the Highly Efficient Adsorption and Regeneration of Acetaldehyde, *J. Mater. Chem. A* 9 (2021) 4066–4074.

[37] R. Liu, W. Zhang, Y. Chen, Y. Wang, Uranium (VI) Adsorption by Copper and Copper/Iron Bimetallic Central MOFs, *Colloid Surf. A* 587 (2020), 124334.

[38] Y. Tang, N. Rong, F. Liu, M. Chu, H. Dong, Y. Zhang, P. Xiao, Enhancement of the Photoelectrochemical Performance of CuWO₄ Films for Water Splitting by Hydrogen Treatment, *Appl. Surf. Sci.* 361 (2016) 133–140.

[39] A.S. Duke, E.A. Dolgopolova, R.P. Galhenage, S.C. Ammal, A. Heyden, M.D. Smith, D.A. Chen, N.B. Shustova, Active Sites in Copper-Based Metal-Organic Frameworks: Understanding Substrate Dynamics, Redox Processes, and Valence-Band Structure, *J. Phys. Chem. C.* 119 (2015) 27457–27466.

[40] H. Zhang, Y. Muhammad, X. Cui, Z. Zhang, L. Liu, Z. Chu, J. Li, Y. Zhang, S.J. Shah, Z. Zhao, Engineering Bidirectional CMC-foam-supported HKUST-1@ graphdiyne with Enhanced Heat/Mass Transfer for the Highly Efficient Adsorption and Regeneration of Acetaldehyde, *J. Mater. Chem. A* 9 (2021) 4066–4074.

[41] H. Park, S. Kim, B. Jung, M.H. Park, Y. Kim, M. Kim, Defect Engineering into Metal-Organic Frameworks for the Rapid and Sequential Installation of Functionalities, *Inorg. Chem.* 57 (2018) 1040–1047.

[42] S.M. Shaikh, P.M. Usov, J. Zhu, M. Cai, J. Alatis, A.J. Morris, Synthesis and Defect Characterization of Phase-pure Zr-MOFs based on Mesotetra-carboxyphenylporphyrin, *Inorg. Chem.* 58 (2019) 5145–5153.

[43] T. Zhao, M. Dong, L. Yang, Y. Liu, Synthesis of Stable Hierarchical MIL-101 (Cr) with Enhanced Catalytic Activity in the Oxidation of Indene, *Catalysts* 8 (2018) 394.

[44] J. Zhou, J. Zhao, R. Liu, Defect Engineering of Zeolite Imidazole Framework Derived ZnS Nanosheets Towards Enhanced Visible Light Driven Photocatalytic Hydrogen Production, *Appl. Catal. B: Environ.* 278 (2020), 119265.

[45] W. Ren, J. Cheng, H. Ou, C. Huang, M. Titirici, X. Wang, Enhancing Visible-Light Hydrogen Evolution Performance of Crystalline Carbon Nitride by Defect Engineering, *ChemSusChem* 12 (2019) 3257–3262.

[46] M. Cabrerero-Antonino, J. Albero, C. García-Vallés, M. Álvaro, S. Navalón, H. García, Plasma-Induced Defects Enhance the Visible-Light Photocatalytic Activity of MIL-125(Ti)-NH₂ for Overall Water Splitting, *Chem. -Eur. J.* 26 (2020) 15682–15689.

[47] A.B. Djurišić, W.C.H. Choy, V.A.L. Roy, Y.H. Leung, C.Y. Kwong, K.W. Cheah, T. K. Gundu Rao, W.K. Chan, H. Fei Lui, C. Surya, Photoluminescence and Electron Paramagnetic Resonance of ZnO Tetrapod Structures, *Adv. Funct. Mater.* 14 (2004) 856–864.

[48] W. Zhen, X. Yuan, X. Shi, C. Xue, Grafting Molecular Cobalt-oxo Cubane Catalyst on Polymeric Carbon Nitride for Efficient Photocatalytic Water Oxidation, *Chem. Asian J.* 15 (2020) 2480–2486.

[49] H. Yang, Z. Jin, H. Hu, Y. Bi, G. Lu, Ni-Mo-S Nanoparticles Modified Graphitic C₃N₄ for Efficient Hydrogen Evolution, *Appl. Surf. Sci.* 427 (2018) 587–597.

[50] B. Dong, T. Liu, C. Li, F. Zhang, Species, Engineering and Characterizations of Defects in TiO₂-based Photocatalyst, *Chinese. Chem. Lett.* 29 (2018) 671–680.